ChemPhysChem

Research Article
doi.org/10.1002/cphc.202300901

Chemistry Europe
European Chemical Societies Publishing

www.chemphyschem.org

Deep Earth Chronicles: High-Pressure Investigation of Phenakite Mineral Be_2SiO_4

Jaspreet Singh,[a] Daniel Errandonea,*[b] Venkatakrishnan Kanchana,*[a] and Ganapathy Vaitheeswaran*[c]

Beryllium silicate, recognized as the mineral phenakite (Be_2SiO_4), is a prevalent constituent in Earth's upper mantle. This study employs density-functional theory (DFT) calculations to explore the structural, mechanical, dynamical, thermodynamic, and electronic characteristics of this compound under both ambient and high-pressure conditions. Under ideal conditions, the DFT calculations align closely with experimental findings, confirming the mechanical and dynamical stability of the crystalline structure. Phenakite is characterized as an indirect band gap insulator, possessing an estimated band gap of 7.83 eV. Remarkably, oxygen states make a substantial contribution to both the upper limit of the valence band and the lower limit of the conduction band. We delved into the thermodynamic properties of the compound, including coefficients of thermal expansion, free energy, entropy, heat capacity, and the Gruneisen parameter across different temperatures. Our findings suggest that Be_2SiO_4 displays an isotropic behavior based on estimated anisotropic factors. Interestingly, our investigation revealed that, under pressure, the compression of phenakite is not significantly affected by bond angle bending.

Introduction

The Earth's mantle is believed to exhibit a Si:O atom ratio that typically falls within the range of 1:3 to 1:4.[1] This has led to significant scientific curiosity regarding the structural characteristics of the orthosilicate group, a category of minerals characterized by the presence of isolated SiO_4 tetrahedra. Research in this field has predominantly focused on examining these minerals under conditions of elevated pressure or temperature. The orthosilicate group encompasses a wide variety of minerals, including olivines, silicate spinels, garnets, aluminosilicates, zircon, and a few less common mineral families like humites and datolites.[2]

Mineralogists have dedicated extensive efforts over the years to uncover a systematic of minerals behaviour, enabling them to make predictions about structures and physical properties under extreme pressure and temperature conditions. One method for discerning these patterns involves experimental analysis of sets of minerals that share similar chemical compositions. In the $BeO–Al_2O_3–SiO_2–H_2O$ system, often referred to as BASH, researchers can discover an ideal combination of abundant, finely shaped, stoichiometric, and well-ordered crystalline phases with diverse structural characteristics. This system produces large, relatively flawless, well-structured crystals in various shapes through its multiple binary and ternary phases. The relatively low atomic numbers of the constituent ions in this system make them amenable to computational quantum chemistry techniques. Across most of the phases in this system, the structural units consist of just three types of cations polyhedra-tetrahedral silicon, beryllium, and octahedral aluminium. This characteristic makes them a perfect case study for the "polyhedral approach".[3]

The X_2YO_4 system is distinguished by its diverse range of compositions, including elements such as X (e.g., Mg, Fe, Mn, Ca, Ni, Co, Zn, Be, Li, Al, Cr, and rare-earth elements) and Y (e.g., Si, Ge, Be, As, B, and P). This system also features extensive solid solution behavior, allowing for mixtures between pure end-member compositions, and exhibits various structure types, such as hexagonal close-packed (hcp) derivatives like olivines ($A_2^{VI}B^{IV}O_4$), cubic close-packed (ccp) spinels ($A^{IV}B_2^{VI}O_4$), the hexagonal phenakite structure, willemite (Zn_2SiO_4), and orthosilicates of cadmium and chromium. This group also includes minerals like silicate spinels, and wadsleyite-type spinelloids. These materials represent some of the simplest "complex" ceramics containing multiple cations, typically composed of only two distinct cation species.

In the BASH system, several minerals, including bromellite (BeO),[4] phenakite (Be_2SiO_4),[5,6] bertrandite ($Be_4Si_2O_7(OH)_2$),[5] beryl ($Be_3Al_2Si_6O_{18}$), euclase ($BeAlSiO_4(OH)$),[7] and chrysoberyl ($BeAl_2O_4$),[8] have been explored by high-pressure crystal

---

[a] J. Singh, Prof. V. Kanchana
Department of Physics
Indian Institute of Technology Hyderabad Kandi
502285 Sangareddy, Telangana, India
E-mail: kanchana@phy.iith.ac.in

[b] Prof. D. Errandonea
Departamento de Fisica Aplicada-ICMUV-MALTA Consolider Team
Universidad de Valencia
C/Dr. Moliner 50, 46100 Burjassot, Valencia, Spain
E-mail: Daniel.Errandonea@uv.es

[c] Prof. G. Vaitheeswaran
School of Physics
University of Hyderabad
Prof. C. R. Rao Road, Gachibowli, Hyderabad-500046, Telengana, India
E-mail: vaithee@uohyd.ac.in

Supporting information for this article is available on the WWW under https://doi.org/10.1002/cphc.202300901

structure investigations. It has been observed that both bromellite and beryl demonstrate a large thermal expansion and the formation of different crystal structures at high temperatures.

The phenakite crystal structure, which was determined by Bragg in 1927, exhibits a well-defined three-dimensional arrangement characterized by tetrahedra of varying types (SiO_4 and BeO_4), each with nearly identical geometric properties, within its structure.[9] In 1972, Zachariasen[10] and in 1983, Downs[11] provided descriptions of the phenakite crystal structure, which is trigonal in nature (belonging to the space group $R\bar{3}$) with a total of 18 formula units per unit cell. Their analysis also included insights into the anisotropic temperature factors. In this structure both silicon and beryllium are tetrahedrally coordinated by oxygen atoms. These tetrahedra are interconnected by their corners, forming a continuous framework featuring rings of three, four, and six members.

In this investigation, we aim to analyse the diverse physical attributes of Be_2SiO_4 and explore how variations in pressure and temperature impact its behavior. The second part of our study delves into the computational details. Moving on to the third section, we provide a comprehensive summary of our key findings and engage in discussions concerning structural properties, elasticity, mechanical behavior, dynamical features, thermodynamics, and electronic properties. We will also discuss these attributes under both ambient and under pressure conditions. Finally, we will consolidate our findings and draw conclusions in the concluding section. The findings of this investigation are relevant for the use of Be_2SiO_4 in Raman lasers.[12]

Computational Methods

The optimization of the molecular geometry of Be_2SiO_4 was performed employing the formalism of density-functional theory (DFT). Computer simulations were carried out using the Vienna Ab initio Simulation Package (VASP)[13] within the projector-augmented wave (PAW) scheme. The Perdew-Burke-Ernzerhof (PBE) for solids (PBEsol)[14] functional was used to generate the exchange-correlation functionals within the context of the Generalized-Gradient Approximation (GGA). Calculations with PBE[14] here were also performed and we concluded that PBEsol describes better the crystal structure of Be_2SiO_4. As a consequence, in this work, we will focus on results of PBEsol calculations unless it is specified. In all calculations, the plane wave energy cutoff was set at 600 eV. We adopted a selected energy convergence criterion of 10^{-8} eV. For geometry optimization computations, a dense k-mesh was utilized following the Monkhorst-Pack technique.[15] To calculate phonon dispersions, we employed the density-functional perturbation theory alongside VASP and Phonopy.[16] The phonon calculations with a 2×2×2 supercell (336 atoms) have been performed using a 6×6×6 k-point mesh and a 10^{-8} eV energy convergence criterion. The thermodynamic properties of the compound under investigation were evaluated using the Quasi-Harmonic approximation, combining VASP and Phonopy.[17] To rectify the underestimate of the GGA approximation when estimating the band gap of semiconductors/insulators,[18] we employed the hybrid functional HSE06 to compute electronic characteristics, setting the Hartree–Fock screening value at 0.2 Å.[19] To analyze the response of the band gap to pressure variations, calculations were conducted using VASP with PBE-GGA potentials. We obtained the bulk modulus and its pressure dependency by fitting the pressure-volume (P–V) data to a third-order Birch-Murnaghan equation of state (EOS) in order to explain how the unit-cell volume reacts to compression.[20]

Results and Discussion

Structural Properties

Phenakite, the mineral Be_2SiO_4, represents the naturally occurring manifestation of the beryllium-silicon binary oxide. As stated in the introduction, the mineral compound Be_2SiO_4 exhibits a trigonal crystalline structure with the space group $R\bar{3}$. Figure 1(a) provides a diagrammatic depiction of the crystal structure. In the current case, the calculations were performed using GGA-PBEsol[14] and GGA-PBE[21] functionals. Our computational analysis shows that GGA-PBEsol functional accurately describes the ground state of the examined compound, as listed in Table 1. Notably, the predicted unit-cell parameters notably align with experimental values,[5,22] showing agreement within a margin of less than 1%. Table 1 shows that PBE tends to slightly overestimate the unit-cell parameters which leads to an overestimation of 27 $Å^3$ of the volume.

The structural arrangement of phenakite consists of a well-organized three-dimensional framework comprising two distinct types of tetrahedra (SiO_4 and BeO_4), which exhibit nearly

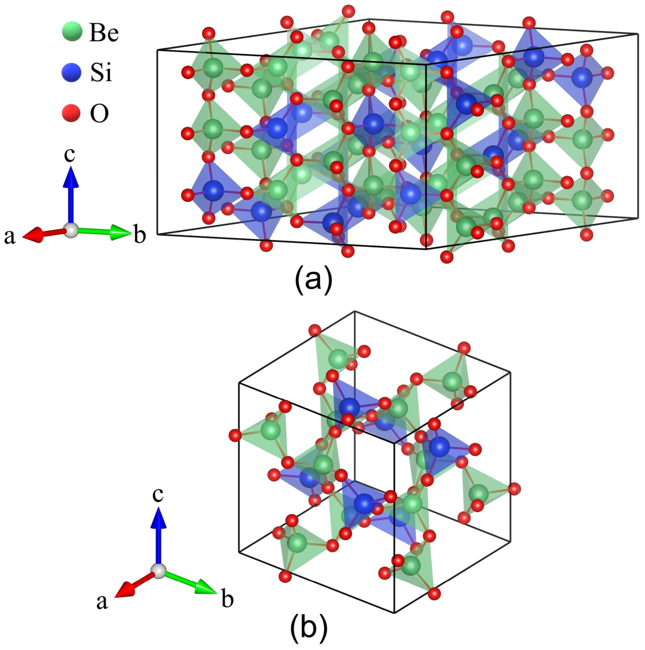

Figure 1. Crystal structure of Be_2SiO_4 (a) conventional cell and (b) primitive cell.

Table 1. Experimental and calculated unit-cell parameters and selected bond distances. For the unit-cell parameters we show results from PBE and PBEsol calculations. The bond-distances are only shown for PBEsol because it gives the best description of the crystal at ambient conditions.

	PBE	PBEsol	Exp.[22]	Exp.[10]	Exp.[5]
a (Å)	12.573	12.494	12.481	12.472	12.470
c (Å)	8.313	8.254	8.261	8.252	8.250
V (Å^3)	1138.11	1115.99	1116.20	1111.63	1111.10
Si–O (Å)	–	1.6424, 1.6390, 1.6456, 1.6410	–	1.6301, 1.6280, 1.6337, 1.6307	1.627, 1.626, 1.629, 1.628
Be1–O (Å)	–	1.6404, 1.6395, 1.6543, 1.6363	–	1.6404, 1.6449, 1.6581, 1.6371	1.639, 1.638, 1.654, 1.642
Be2–O (Å)	–	1.6305, 1.6381, 1.6535, 1.6534	–	1.6310, 1.6431, 1.6553, 1.6546	1.633, 1.637, 1.655, 1.652

identical geometrical characteristics. Tetrahedra interconnect to form chains aligned with the crystallographic threefold axis, generating spacious hexagonal channels. Inside the phenakite crystal's unit cell, there is a silicon atom occupying one Wyckoff position, as well as two distinct beryllium atoms and four distinct oxygen atoms. A planar trigonal arrangement is formed by one Si atom and two Be atoms, each coordinating with an oxygen atom. In terms of hexagonal axes, the standard non-primitive unit cell accommodates 18 formula units, and the atoms reside in general positions (exhibiting site symmetry 1). Be_2SiO_4 falls into the category of neso-silicates due to the isolation of [SiO_4] coordination polyhedra from each other within the crystal structure. However, the strong bonding interaction with [BeO_4] imparts a structural resemblance more akin to framework structures, akin to tecto-silicates. The average cation-anion bond lengths for the three distinct tetrahedra: Si, Be1, and Be2 polyhedra, are 1.642 Å, 1.643 Å, and 1.644 Å, respectively (as indicated in Table 1). These tetrahedra exhibit minimal deformation, with quadratic elongation (QE) and angle variance (AV) closely approaching the ideal values (as presented in Table 2).

Moreover, we have computed the structural parameters as pressure-dependent variables and shown in Figure 2(a). We observed that the volume (V/V_0) and lattice parameters (a/a_0, c/c_0) correspond well with experiments[22] up to 10 GPa. At this pressure there is a small reduction of compressibility in experiments which is not accounted by calculations. This may be attributed to the use of a 16:3:1 methanol-ethanol-water mixture as a pressure-transmitting medium in powder X-ray diffraction experiments.[18] This pressure-transmitting medium remains quasi-hydrostatic only until 10 GPa.[23] It is a commonly recognized phenomenon that non-hydrostatic compression can artificially reduce the compressibility of a crystal.[24] In fact, in the X-ray diffraction experiments reported in Ref. [22] the peaks at 10.3 GPa are considerably broad, a fingerprint of the impact of non-hydrostatic effects. The results revealed that the compression of lattice parameters *a* and *c* are similar. The linear compressibility of the two lattice parameters is $k_a = 1.75\times10^{-3}\ GPa^{-1}$ and $k_c = 1.59\times10^{-3}\ GPa^{-1}$ *i.e.*, *c* parameter is slightly less compressible than *a* parameter. Our results agree with those determined by Hazen and Au[5] from single-crystal X-ray diffraction experiments performed up to 5 GPa, $k_a = 1.60(3)\times10^{-3}\ GPa^{-1}$ and $k_c = 1.45(7)\times10^{-3}\ GPa^{-1}$. In contrast, Fan *et al.*,[22] determined smaller values for each linear compressibility, $k_a = 1.50\times10^{-3}\ GPa^{-1}$ and $k_c = 1.34\times10^{-3}\ GPa^{-1}$, which is an artifact of the non-hydrostatic conditions of experiments at 10.3 GPa and higher pressures.

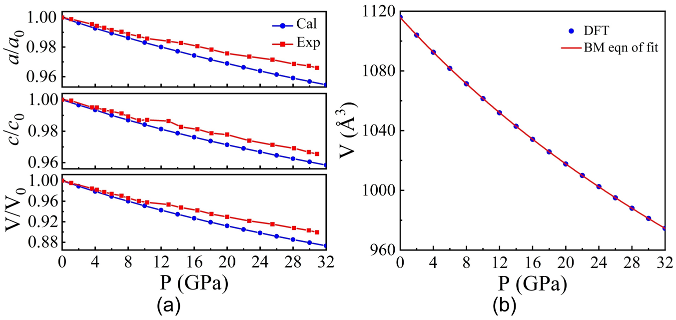

Figure 2. Pressure dependence of (a) lattice parameters and volume, and (b) volume along with BM equation fit. In (a) we compare with previous experiments.[22] In (b) the symbols are the results from our calculations and the red line correspond to the EOS with parameters $V_0 = 1116.0$ Å^3, $B_0 = 181.7$ GPa, and $B_0' = 3.87$.

In addition, to linear compressibilities, the volume (V_0), the bulk modulus (B_0) and its pressure derivative (B_0') at zero pressure were determined through least-squares analysis of pressure-volume results. To determine the bulk modulus for the orthosilicate, we employed the third-order Birch-Murnaghan equation of state (EOS).[20] The resulting V_0, B_0, and B_0' for phenakite are 1116.0 Å^3, 181.7 GPa, and 3.87, respectively. In Figure 2(b), the unit-cell volume data plotted against pressure is depicted, along with the pressure-volume curve determined using these fitted parameters. Hazen and Au[5] have obtained $B_0 = 201(8)$ GPa and $B_0' = 2(4)$. The B_0' is unusually small for a

Table 2. Polyhedral volumes (V_P in Å^3), quadratic elongation (QE) of bond-distances, and angles variance (AV) for the Be1, Be2, and Si coordination polyhedral of phenakite at zero pressure.

	Be1			Be2			Si		
	V_P	QE	AV	V_P	QE	AV	V_P	QE	AV
Cal.	2.270	1.001	4.7	2.275	1.002	6.2	2.269	1.001	3.9
Exp.[5]	2.279	1.001	6.0	2.284	1.002	7.2	2.218	1.001	4.1

silicate.[25] If the data from Hazen and Au[5] are fitted using a 2nd order Birch–Murnaghan EOS ($B_0'=4$), $B_0=195(11)$ GPa. This means that our results agree within two standard deviations with the experiments from Hazen and Au.[5] In contrast, in the EOS determined from the experiments of Fan *et al.*[22] $B_0=223(9)$ GPa and $B_0'=5.5(8)$ are overestimated due to the influence of non-hydrostatic effects.[26]

Pressure induces changes in both the distinct cation polyhedra and the angles between them, offering valuable insights into the response of the phenakite structure. Figure 3(a) and Supplementary Figure S1 display the changes in selected interatomic bond lengths and angles with respect to pressure variation. In the phenakite structure, all three tetrahedra experience substantial compression which is shown in Figure 3(b–d). The polyhedra respond to pressure predominantly by undergoing volumetric compression, and this has a minimal effect on their distortions. This is evident from the consistently stable quadratic elongation and angle variance observed throughout the pressure range examined in our study.

In solid materials that comprise cation polyhedra, compression arises from the interplay between polyhedral compression and changes in inter-polyhedral angles. When considering the investigated compound (phenakite), the Si–O–Si and Be–O–Be angles are consistently near 120° and remain virtually unchanged within one estimated standard deviation between ambient pressure and 32 GPa. This implies that the compression of phenakite is not significantly influenced by the bond angle bending and the polyhedral tilting. These results show that the conclusions obtained by Hazen and Au[5] regarding the mechanism of compression are valid up to 32 GPa.

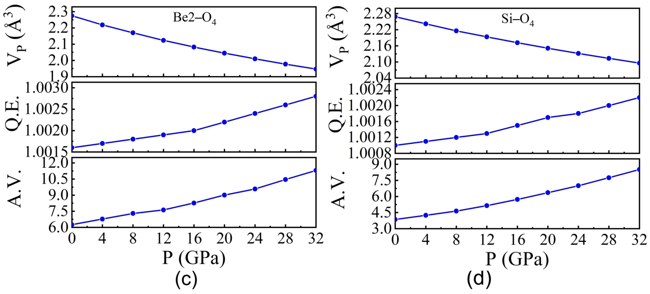

(a) (b)
(c) (d)

Figure 3. Pressure dependence of (a) selected bond distances, and (b–d) polyhedral volume along with the quadratic elongation (QE) and angular variance (AV) of Be1, Be2 and Si tetrahedral units.

To conclude the discussion of this section we would like to compare the bulk modulus from Be_2SiO_4 with the bulk modulus from other beryllium minerals. The bulk modulus of Be_2SiO_4, 182–195 GPa, is slightly smaller than that of $BeAl_2O_4$, 213 GPa[27] and that of BeO, 212 GPa.[4] This suggest that the incorporation of silicon favors a decrease of the bulk modulus while the incorporation of aluminum does not. This conclusion is consistent with the facts that the bulk modulus of $Be_3Al_2Si_6O_{18}$, with a larger Si/Be ratio, is 170 GPa[7] and the bulk modulus of $CsBe_4Al_4(B_{11}Be)O_{28}$, which contains Al, Cs, and B, but not Si, is 213 GPa;[28] *i.e.* identical to that of BeO and $BeAl_2O_4$. Based on this observation we speculate that $BeSiO_3$ (Si/Be ratio = 1) will have a bulk modulus smaller than that of Be_2SiO_4 (Si/Be ratio = 1/2) and larger than that of $Be_3Al_2Si_6O_{18}$ (Si/Be ratio = 2), and that $Be_2Al_2Si_5O_{15}$ (Si/Be ratio = 5/2) will have a bulk modulus smaller than $Be_3Al_2Si_6O_{18}$.

Elastic and Mechanical Properties

Elastic constants play a crucial role in comprehending the mechanical characteristics, including stability under external loads. In our case, we employed the first-principles approach to estimate the elastic constants C_{ij} based on the equilibrium cell characteristics and determined C_{ij} are tabulated in Table 3. The computed C_{ij} closely align with the experimental results.[29] The C_{ij} acquired at all pressures examined in this study adhere to the generalized Born-Huang criteria,[30,31] indicating the material's mechanical stability. Accordingly, Be_2SiO_4 was identified as a mechanically stable material by applying the mechanical stability criterion. On the other hand, to deduce the linear stability of our compound, we have calculated the eigen-values of the elasticity tensor. The computed eigen-values are: $\lambda_1=544.09$, $\lambda_2=284.13$, $\lambda_3=174.99$, $\lambda_4=82.25$, $\lambda_5=82.24$, and $\lambda_6=87.51$ GPa. The ratio of $\lambda_{max}/\lambda_{min}$ is 6.62 which is higher than 1 and it indicates that the structure is stiffer. In order to attain a more profound understanding into how the material behaves in high-pressure conditions, we assessed the elastic constants at both ambient and elevated pressures, as shown in Figure 4(a). It is a widely recognized fact that the C_{11} and C_{33} provide information about the material's resistance to linear compression along the crystallographic *a*- and *c*-axes, respectively. The obtained values of the C_{ij} reveal that C_{33} is greater than C_{11}, indicating that the studied compound exhibits slightly more compressibility along the *a*-axis than the *c*-axis, as discussed in the previous section. The elastic constants (C_{11} and C_{33}), which measure stiffness in response to uniaxial strains,

Table 3. The elastic constants C_{ij} (in GPa) at ambient conditions.

	C_{11}	C_{33}	C_{44}	C_{12}	C_{13}	C_{14}	C_{15}
Cal.	311.87	379.47	82.25	136.88	88.59	0.21	0.08
Exp.[29]	341.9	391.0	91.4	148.0	136.0	0.1	3.5

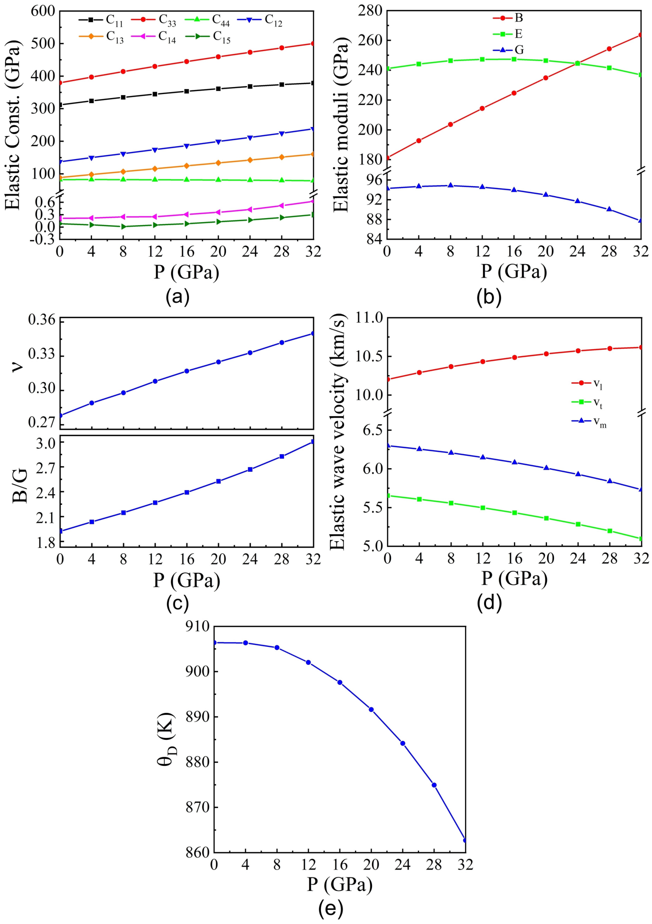

Figure 4. Pressure dependence of (a) Elastic constants, (b) elastic moduli, (c) Poisson's ratio and B/G values, (d) elastic wave speed, and (e) Debye temperature.

exhibit high values, whereas the elastic constant (C_{44}), representing resistance to shear deformation *i.e.*, C_{44} represents rigidity in the *a–c* plane, requires shearing in a direction that's perpendicular to the tetrahedral chains, is notably low. Thus, according to this low value of C_{44}, Be_2SiO_4 is more resistive to compressive or tensile deformations than to shear ones.[32] In this case, the tetrahedra can rotate when subjected to a C_{44}-type shear. In addition, the elastic constant C_{66} quantifies a material's ability to withstand stress that tries to separate the tetrahedral chains extending perpendicular to the *a*-axis, which is a more challenging type of shear to achieve. The elastic constant C_{66} can be calculated using C_{11} and C_{12} i.e., $(C_{11}–C_{12})/2$. The calculated values of C_{44} and C_{66} show that $C_{66} > C_{44}$. The higher shear rigidity observed in elastic modulus C_{66} within the basal plane can be attributed to the triangular voids, which function as cross braces. In contrast, elastic modulus C_{44} does not account for this specific type of shear behaviour. Hence, the rigidity of the tetrahedral structure plays a more direct role in determining elastic modulus C_{66} compared to elastic modulus C_{44}.[29]

The determination of polycrystalline bulk (B) and shear modulus (G) relies on the elastic constants. We employed two approximation methods for calculating these moduli: (a) the Voigt method and (b) the Reuss method.[33] According to Hill's methodology,[34] the bulk modulus can be expressed as the average of the Voigt bulk modulus (B_V) and the Reuss bulk modulus (B_R), and similarly, the shear modulus is determined as the average of the shear moduli (G_V) and (G_R).[35] These bulk and shear moduli can then be employed to derive Young's modulus (E) and Poisson's ratio (ν). The computed elastic moduli, in conjunction with the experimental findings, are listed in Table 4. The calculated B value at zero pressure, 181.21 GPa, aligns with the B_0 value derived using the Birch-Murnaghan EOS, 181.7 GPa. The elastic properties of Be_2SiO_4 are found to intermediate to the bromellite[36] and beryl[37] minerals. In Figure 4(b), it is evident that the computed B values exhibit an upward trend as pressure increases, while the G and E values display an initial increase followed by a subsequent decrease after reaching a certain point. This means that at pressures higher than those cover by this study there will develop mechanical instabilities triggering either a phase transition or amorphization.[38]

Ductility and brittleness are pivotal mechanical characteristics of any material. In accordance with empirical criteria,[39–41] when a solid exhibit $\nu < 0.26$ and $B/G < 1.75$, it falls into the category of brittleness; otherwise, it is considered ductile. Our calculated values for B/G and ν are both above 1.75 and 0.26, respectively. As a result, the investigated compound demonstrates ductile nature. This phenomenon can be mainly associated to the lower value of the G in comparison to other silicates, such as $MgSiO_3$.[42] Furthermore, these values signify the prevalence of ionic contributions in inter-atomic bonding across all the compounds. To fully confirm this statement, calculations of the non-covalent index are needed. However, they are beyond the scope of this work and will be addressed in future studies. In addition, we have calculated the pressure dependence of ν and B/G ratio which is shown in Figure 4(c). The Figure 4(c) illustrates an increase in both B/G and ν as pressure varies from 0 GPa to 32 GPa. Furthermore, Pettifor's criterion[43] introduces the concept of Cauchy's pressure ($C_{13}–C_{44}$ and $C_{12}–C_{66}$) to determine a material's brittle or ductile nature. When Cauchy's pressure is in the negative range, the material displays brittleness, whereas when it's positive, the material exhibits ductile behaviour. Thus, according to the Cauchy's pressure, our compound is ductile.

Table 4. The experimental and calculated elastic properties of Be_2SiO_4.

	B (GPa)	E (GPa)	G (GPa)	ν	v_l (km/s)	v_t (km/s)	v_m (km/s)
Cal.	181.21	241.05	94.29	0.278	10.20	5.65	6.30
Exp.[29]	212.8		98.9		10.79	5.74	8.47

Crystals with low symmetry often exhibit pronounced elastic anisotropy. Information regarding the extent of this anisotropy can be obtained by examining shear anisotropy factors across various crystallographic planes. Elastic constants can be employed to calculate shear anisotropic factors on the (100)/(010) and (001) planes ($A_1 = A_2$, and A_3).[44] If the shear anisotropic factor equals one, the material is considered isotropic. Conversely, Chung and Buessem[45] suggest that the proportion of anisotropy in bulk (A_B) and shear modulus (A_G) can be used to quantify elastic anisotropy. To assess an anisotropic nature of a crystal, Ranganathan and Ostoja-Starzewski[46] proposed a universal anisotropy factor (A^U). The material exhibits isotropic characteristics when A_B, A_G, and A^U approach zero. In this context, Table 5 presents A_1, A_3, A_B, A_G, and A^U values of Be_2SiO_4. The estimated values of these parameters suggest that the compound Be_2SiO_4 exhibits a subtle anisotropic behaviour, aligning with the findings from the pressure-dependent assessment of *a* and *c*.

Elastic constants play a pivotal role in determining sound velocities. We employed Navier's equation to determine the longitudinal (v_l), transverse (v_t), and mean sound velocities (v_m) under both standard and high-pressure conditions. Table 4 indicates that our calculated wave velocities are in excellent accordance with the experimental findings.[29] The calculated sound velocities are illustrated in Figure 4(d). With increasing pressure, the estimated values of v_l demonstrate an upward trend. On the other hand, v_t and v_m show downward trend at high-pressure. Another significant parameter to consider is the Debye temperature (θ_D), which varies in relation to the average sound velocities. The results obtained from the Debye-Grunesien model are depicted in Figure 4(e), illustrating the variations in Debye temperature as pressure increases. In Figure 4(e), the fluctuation of the Debye temperature under high pressure is visually depicted, showcasing a corresponding decrease with increasing pressure.

Lattice Dynamics and Thermodynamic Properties

Phonon dispersion analysis was performed along the high-symmetry path (Γ–M–K–Γ–A) under zero pressure to evaluate the material's dynamical stability. The calculated phonon dispersion is shown in Figure 5(a) and 5(b). Our results indicated that the acoustic branches display positive frequencies, affirming the dynamical stability of the analysed system. Notably, there is a pronounced interaction between the optical and acoustic modes, which can be attributed to the similar atomic masses of the constituent entities. In addition, we have calculated the phonon dispersion at 32 GPa which is shown in Figure 5(c) and 5(d). The phonon dispersion shows that all phonon modes are positive, which support the stability of the material at 32 GPa. In the section on structural properties, we previously explored how pressure results in the shortening of bond lengths. This compression of the crystal leads to a widening of frequency band gaps. Consequently, as molecules get closer, there is a resultant repulsion between atoms. The impact of pressure becomes evident in the splitting of branches and an increase in their dispersion. Furthermore, branches exhibit an upward shift along the frequency axis with rising pressure. Notably, as pressure increases, the acoustic branches near point Γ display an enhanced slope. This signifies a heightened sonic velocity, a consequence of the crystal's density increasing under compression.

Moreover, we have computed the vibrational modes at zero pressure and provided in Table 6. Table 6 clearly exhibits the presence of 126 vibrational bands, consistent with the experimental findings.[47] The mechanical representation of these modes is: $\Gamma_M = 21A_g + 21A_u + 21E_g + 21E_u$. Here, the E_g and E_u modes are doubly degenerate modes. The calculated modes contain the 63 Raman active ($21A_g + 21E_g$), 3 acoustic ($A_u + E_u$) and 60 IR active ($20A_u + 20E_u$) modes. The acquired mode values closely match both the experimental results[47,48] and the outcomes from the Born-von Karman rigid-ion lattice-dynamical model.[49] In phenacite, the vibrational bands are assigned to specific modes as follows: Above 919 cm^{-1}, the observed bands are attributed to the bending (Si–O) mode. In the range between 840 and 800 cm^{-1}, the bands are associated with the symmetric (Si–O) stretching mode. Bands falling within the 440–350 cm^{-1} region are indicative of the asymmetric (Si–O) stretching mode. The bands spanning from 576 to 430 cm^{-1} are a manifestation of the rocking (Si–O) stretching mode.

Table 5. Shear anisotropy factors defined in the text at different pressures.

P (GPa)	A_1	A_3	A_B ($\times 10^{-3}$)	A_G	A^U
0	0.640	1	0.268	0.022	0.223
4	0.628	1	0.296	0.024	0.248
8	0.614	1	0.349	0.027	0.274
12	0.603	1	0.394	0.029	0.303
16	0.594	1	0.454	0.032	0.334
20	0.585	1	0.524	0.035	0.369
24	0.579	1	0.601	0.039	0.409
28	0.572	1	0.698	0.044	0.461
32	0.566	1	0.808	0.050	0.532

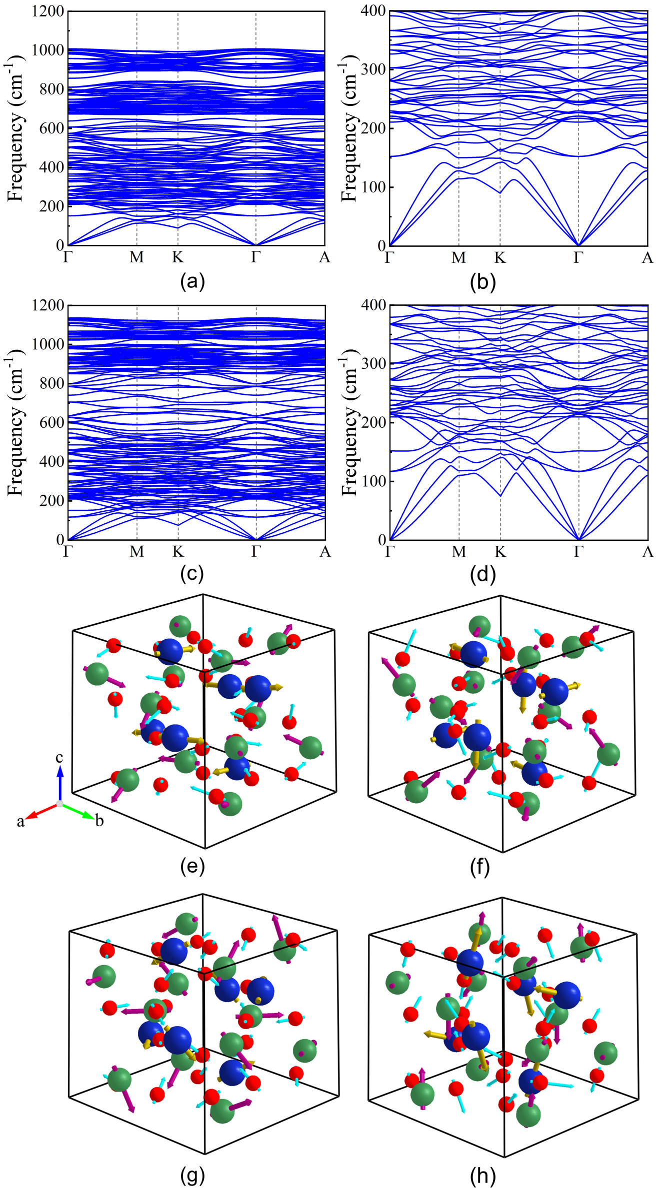

(a) (b) (c) (d) (e) (f) (g) (h)

Figure 5. The phonon dispersion (at 0 GPa) in (a) full range and (b) low dispersion range. The phonon dispersion (at 32 GPa) in (c) full range and (d) low dispersion range. The calculated phonon modes at selected frequencies (at 0 GPa): (e) E_g – 366.38 cm^{-1}, (f) A_u – 531.36 cm^{-1}, (g) A_g – 811.32 cm^{-1} and (h) E_u – 1004.61 cm^{-1}.

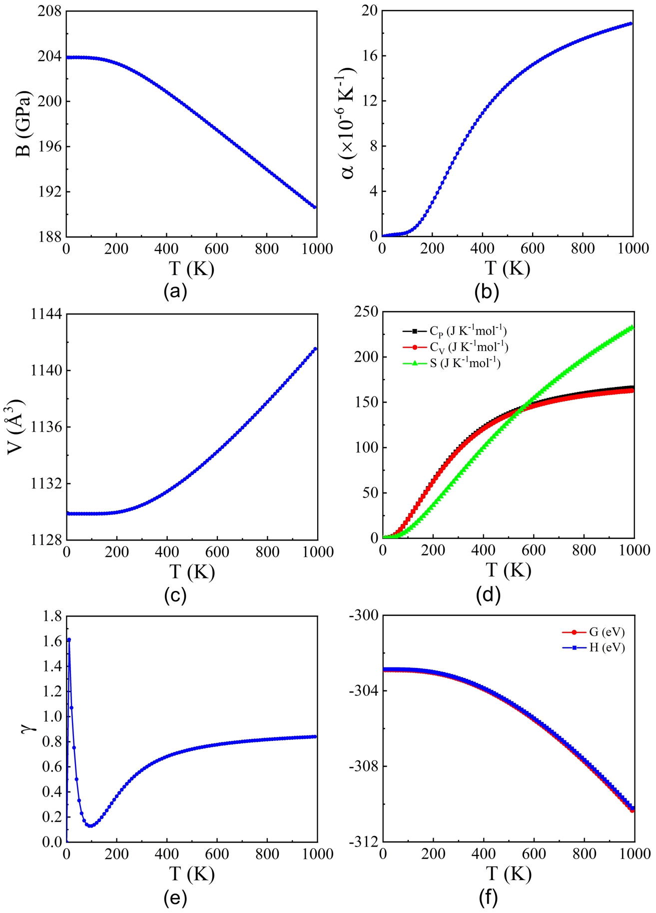

(a) (b) (c) (d) (e) (f)

Figure 6. Bulk modulus, thermal expansion, volume expansion, C_P, C_V, entropy, Gruneisen parameter, Gibbs free energy and free energy as a function of temperature.

Additionally, a feature appearing at around 770 cm^{-1} is linked to the symmetric stretching of Be–O bonds.[50] Figure 5(e–h) illustrates a selection of few vibrational modes at 0 GPa.

The thermodynamic properties were computed using the Phonopy code, which relies on the quasi-harmonic approximation as its fundamental framework. Figure 6 presents several predicted thermodynamic parameters, including the B, thermal expansion coefficients (α), volume expansion, specific heat at constant volume (C_V) and pressure (C_P), entropy (S), Gibbs free energy (G), Gruneisen parameter (Υ), and free energy (H) at different temperatures. Figure 6(a) specifically depicts the temperature-dependent changes in the B. It is apparent from Figure 6(a) that the B decreases with increasing temperature, highlighting the material's compressible characteristics due to the lower B value. The system exhibits a positive α, as evidenced by the temperature-dependent α presented in Figure 6(b). The α at 300 K corresponds well with the experimental value, with a calculated value of 7.4×10^{-6} K^{-1} closely matching the experimental measurement of 9×10^{-6} K^{-1}.[51] Figure 6(c) illustrates computed volume expansion, providing insights into how the material responds to changes in temperature. Specific heat capacity, which quantifies a substance's ability to store heat, is depicted in Figure 6(d), showing computed values for C_P, C_V, and entropy at high temperatures. Our determined C_P value at 300 K is 98.29 J mol^{-1} K^{-1} which is almost equal to the experimental value 95.55 J mol^{-1} K^{-1}. Furthermore, the S value at 300 K, which is 68.73 J mol^{-1} K^{-1}, closely matches the experimental data of 63.37 J mol^{-1} K^{-1}.[52] Figure 6(d) reveals that the value of S is zero at 0 K and increases rapidly with rising temperature. As depicted in Figure 6(d), the specific heat values C_P and C_V exhibit a nearly indistinguishable trend with temperature. At lower temperatures, the specific heat rises sharply, while the variation is

Table 6. Calculated frequencies ω (cm^{-1}) of vibrational modes of Be_2SiO_4.

Mode	ω Cal.	ω Exp.[47,48]	ω Cal.[49]	Mode	ω Cal.	ω Exp.[47,48]	ω Cal.[49]
E_g	152.41	161	174	A_g	210.73		213
	220.86	222	225		240.15		245
	244.08		257		246.08		248
	266.11		277		263.44		272
	333.30		347		283.02		310
	366.38	384	388		391.52		416
	425.58		457		413.65		424
	444.88	446	496		428.07		460
	504.61	523	539		461.69		468
	564.06		577		475.20		505
	606.92		614		574.58		640
	676.76	687	675		682.53		713
	701.70		707		707.82		723
	721.44		720		717.69		730
	731.01		734		770.62	787	748
	776.01		774		791.81		805
	810.43		846		811.32		853
	903.72		920		856.37	879	881
	923.47	928	926		907.40		918
	980.64		970		931.95	952	943
	999.56		999		990.57	1020	956
E_u	226.95		235	A_u	217.25		234
	280.57		284		229.74		260
	303.03		308		259.00		273
	341.85		353		281.78		309
	355.91	358	381		326.42	361	385
	399.64		445		410.54	431	410
	420.06	435	471		452.63		494
	502.01		530		531.36	545	526
	541.73		569		553.53	579	580
	573.84	600	600		637.98	643	639
	689.53	704	695		673.39		649
	698.22	716			695.50		696
	712.43	733	733		719.47		712
	746.41		778		735.56	739	744
	778.11	768	798		748.81	791	820
	793.65	808	831		797.51	840	837
	884.25	917	899		888.61	908	925
	920.29		935		911.08	964	963
	957.64	965	973		987.30	997	983
	1004.61	1110	1077		1007.32	1104	1073

minor at higher temperatures. Importantly, the C_V follows the Dulong-Petit law at elevated temperatures. Figure 6(f) showcases the changes in G and H at higher temperatures, revealing a decrease as the temperature rises. The ϒ, presented in Figure 6(e), display a consistent positive trend across all temperature ranges.

Electronic Properties

To comprehensively characterize the physical attributes of our investigated compound, we calculated the electronic structure calculations utilizing the GGA–PBEsol functional, which yielded a band gap of 5.84 eV as presented in Figure 7(a). Our calculated band gap is almost equal to the earlier reported band gap (6.007 eV), which was determined by FLAPW method using the GGA–PBE functional.[53] Given the well-known tendency of GGA to underestimate band gaps in insulators and semiconductors,[18] we applied the HSE06 functional to enhance the accuracy of band gap. Figure 7(c) shows that the determined band gap is around 7.83 eV. The system under investigation is an indirect gap insulator, as illustrated by the band structure, where the highest point of the valence band and the lowest point of the conduction band are positioned at distinct locations. Nevertheless, the energy gap between the direct transition and the indirect transition is quite minimal. Furthermore, the analysis of the band structure reveals that there is minimal dispersion in the valence band, whereas the conduction band displays significant dispersion.

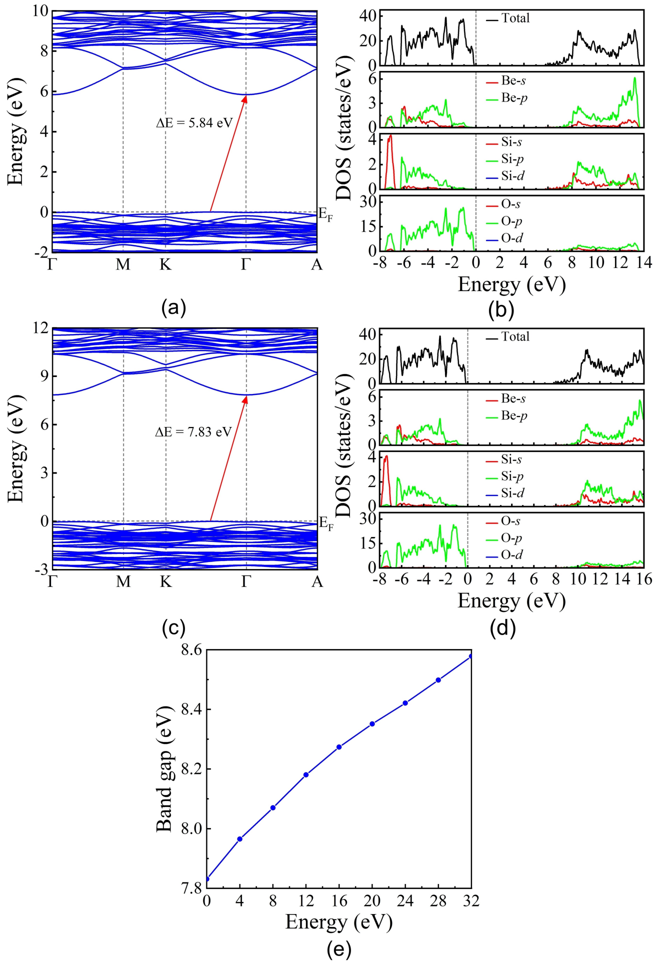

(a) (b)

(c) (d)

(e)

Figure 7. The electronic band structure and projected density of states using (a–b) PBEsol-GGA and (c–d) HSE functionals. (e) Pressure dependence of band gap (with HSE).

For a more in-depth understanding of the electronic properties, we have determined the total and partial density of states (DOS), which are represented in Figure 7(b) (with GGA) and 7(d) (with HSE06). From the Figure 7(d), we can observe that, within the valence band, there exist two manifolds. One of these manifolds extends from −7.89 eV to −6.95 eV and another one extends from −6.53 eV to the Fermi level. The first manifold in the valence band exhibits minimal dispersion (as illustrated in Figure 7(d)), is predominantly comprised of O-2*p* states. However, it also displays significant contributions from the Si-3*s* states. On the other hand, the second manifold mainly possesses O-2*p* states, with minor contributions from Si-3*p*, Be-2*s*, and Be-2*p* states. These two manifolds within the valence band are distinguished by a quasi-band gap of approximately 0.42 eV. According to the earlier reported DOS in Ref.,[53] the primary contributors to the highest peak of the valence band and the lowest peak of the conduction band in the Be_2SiO_4 compound are primarily oxygen states. We have also noted that the primary contributions to the upper valence band and the lower conduction band mainly originate from oxygen states. In this regards the bandgap of Be_2SiO_4 is comparable to that of X_2SiO_4 silicates, which all have a bandgap larger than 6 eV, and a similar contribution of O-2*p* and Si-3*s* orbitals to states at the bottom of the conduction band and the top of the valence band.[54] This characteristic is also shared by other silicates like SiO_2 and $XSiO_3$ perovskites, being the only exception $BaSiO_3$, with a "narrow" bandgap of 4.1 eV due to the contribution of Ba-6*s* orbitals to states near the Fermi level.[55]

Furthermore, we conducted high-pressure calculations to explore the electronic properties under varying pressure conditions. As the pressure increases, there is a substantial rise in the band gap, as illustrated in Figure 7(e). This can mainly be ascribed to the elevation in the crystal field and the expansion of the separation between bonding and antibonding states.[56]

Conclusions

In summary, we conducted a comprehensive investigation into the structural and physical properties of the mineral phenakite using first-principles calculations. Our determined structural parameters align favorably with experimental measurements available, affirming the accuracy of our approach. In addition, as pressure increased, we observed a gradual reduction in volume, lattice parameters, and significant bond lengths, signifying the pronounced impact of pressure on the atomic structure. Notably, the compression of lattice parameters *a* and *c* displayed a nearly isotropic behavior. Furthermore, our analysis encompassed the electronic band gap, spanning from 0 GPa to 32 GPa. It was evident that as pressure increased, there was a notable rise in the band gap. Concurrently, the Bulk modulus exhibited an increase under pressure, while the Shear modulus and Young's modulus experienced a decrease with rising pressure. The computed frequencies of vibrational modes, which include 63 Raman active modes, 3 acoustic modes, and 60 IR active modes, exhibit a strong agreement with prior Raman and infrared experiments conducted under ambient conditions. We also explored the calculation of different thermodynamic properties with respect to temperature. In the quasi-harmonic approximation, we determined that thermal expansion was positive. In conclusion, our calculations provide a comprehensive assessment of the diverse physical characteristics of Be_2SiO_4.

Supporting Information

The supporting information contains the information of the selected bond angles as a function of pressure.

Acknowledgements

The authors J.S and V.K. acknowledge the National Supercomputing Mission (NSM) for providing computing resources of 'PARAM SEVA' at IIT Hyderabad. V. K. would like to acknowledge DST-FIST (SR/FST/PSI-215/2016) for the financial support. J. S. would like to acknowledge CSIR for the fellowship. D. E. thanks the financial support from the Spanish Ministerio de Ciencia e Innovación (https://doi.org/10.13039/501100011033) under Projects PID2019-106383GB-41, PID2022-138076NB-C41, and RED2022-134388-T. D. E. also thanks the financial support of Generalitat Valenciana through grants PROMETEO CIPROM/2021/075-GREENMAT and MFA/2022/007. This study forms part of the Advanced Materials program and is supported by MCIN with funding from European Union Next Generation EU (PRTR-C17.I1) and by the Generalitat Valenciana. G. V. would like to acknowledge Institute of Eminence, University of Hyderabad (UoH-IoE-RC3-21-046) for funding and CMSD University of Hyderabad for providing the computational facility.

Conflict of Interests

The authors declare no conflict of interest.

Data Availability Statement

The data that support the findings of this study are available from the corresponding author upon reasonable request.

Keywords: Phenakite · Ab-initio calculation · High-pressure study · Thermodynamic properties · Electronic band structure

[1] J. Ita, L. Stixrude, *J. Geophys. Res. [Solid Earth]* **1992**, *97*, 6849–6866.

[2] W. A. Deer, R. A. Howie, J. Zussman, *Rock-Forming Minerals, Vol. 2B, Double-Chain Silicates (2nd Edition)*, Geological Society of London, **1997**.

[3] R. M. Hazen, *Rev. Mineral.* **1985**, *14*, 317–346.

[4] R. M. Hazen, L. W. Finger, *J. Appl. Phys.* **1986**, *59*, 3728–3733.

[5] R. M. Hazen, A. Y. Au, *Phys. Chem. Miner.* **1986**, *13*, 69–78.

[6] T. Kogure, Y. TakÉuchi, *Mineral. J.* **1986**, *13*, 22–27.

[7] R. M. Hazen, A. Y. Au, L. W. Finger, *Am. Mineral.* **1986**, *71*, 977–984.

[8] R. M. Hazen, *Phys. Chem. Miner.* **1987**, *14*, 13–20.

[9] W. L. Bragg, *Proceedings of the Royal Society of London. Series A, Containing Papers of a Mathematical and Physical Character* **1927**, *A113*, 642–657.

[10] W. H. Zachariasen, *Sov. Phys. Crystallogr.* **1972**, *16*, 1021–1025.

[11] J. W. Downs, *An experimental examination of the electron disterbution in bromellite, BeO, and phenacite, Be2SiO4*, PhD Thesis, Virginia Polytechnic Institute and State University, Blacksburg, Virginia, **1983**.

[12] A. A. Kaminskii, O. Lux, H. Rhee, H.-J. Eichler, H. Yoneda, A. Shirakawa, P. Becker, L. Bohatý, *Laser Photonics Rev.* **2014**, *8*, 324–331.

[13] G. Kresse, J. Furthmüller, *Comput. Mater. Sci.* **1996**, *6*, 15–50.

[14] J. P. Perdew, A. Ruzsinszky, G. I. Csonka, O. A. Vydrov, G. E. Scuseria, L. A. Constantin, X. Zhou, K. Burke, *Phys. Rev. Lett.* **2008**, *100*, 136406.

[15] H. J. Monkhorst, J. D. Pack, *Phys. Rev. B* **1976**, *13*, 5188–5192.

[16] X. Gonze, C. Lee, *Phys. Rev. B: Condens. Matter Mater. Phys.* **1997**, *55*, 10355–10368.

[17] A. Togo, L. Chaput, I. Tanaka, G. Hug, *Phys. Rev. B* **2010**, *81*, 174301.

[18] T. Ouahrani, R. M. Boufatah, M. Benaissa, Á. Morales-Garcia, M. Badawi, D. Errandonea, *Phys. Rev. Mater.* **2023**, *7*, 25403.

[19] J. Heyd, G. E. Scuseria, M. Ernzerhof, *J. Chem. Phys.* **2003**, *118*, 8207–8215.

[20] F. Birch, *Phys. Rev.* **1947**, *71*, 809–824.

[21] J. P. Perdew, K. Burke, M. Ernzerhof, *Phys. Rev. Lett.* **1996**, *77*, 3865–3868.

[22] D.-W. Fan, M.-N. Ma, S.-Y. Wei, Z.-Q. Chen, H.-S. Xie, *Chin. Phys. C* **2012**, *36*, 179.

[23] S. Klotz, J.-C. Chervin, P. Munsch, G. Le Marchand, *J. Phys. D* **2009**, *42*, 75413.

[24] A. B. Garg, D. Errandonea, *J. Solid State Chem.* **2015**, *226*, 147–153.

[25] T. S. Sokolova, P. I. Dorogokupets, *Minerals* **2021**, *11*, 322, DOI 10.3390/min11030322.

[26] P. Wang, D. He, C. Xu, X. Ren, L. Lei, S. Wang, F. Peng, X. Yan, D. Liu, Q. Wang, L. Xiong, J. Liu, *J. Appl. Phys.* **2014**, *115*, 43507.

[27] J. Singh, V. K. Sharma, V. Kanchana, G. Vaitheeswaran, D. Errandonea, *Mater. Today Commun.* **2021**, *26*, 101801.

[28] G. D. Gatta, P. Lotti, D. Comboni, M. Merlini, P. Vignola, H.-P. Liermann, *J. Am. Ceram. Soc.* **2017**, *100*, 4893–4901.

[29] A. Yeganeh-Haeri, D. J. Weidner, *Phys. Chem. Miner.* **1989**, *16*, 360–364.

[30] M. Born, in *Mathematical Proceedings of the Cambridge Philosophical Society*, **1940**, pp. 160–172.

[31] F. Mouhat, F.-X. Coudert, *Phys. Rev. B* **2014**, *90*, 224104.

[32] N. Guechi, A. Bouhemadou, R. Khenata, S. Bin-Omran, M. Chegaar, Y. Al-Douri, A. Bourzami, *Solid State Sci.* **2014**, *29*, 12–23.

[33] A. Reuß, *ZAMM-Journal of Applied Mathematics and Mechanics/Zeitschrift für Angewandte Mathematik und Mechanik* **1929**, *9*, 49–58.

[34] R. Hill, *Proc. Physi. Soc. Sect. A* **1952**, *65*, 349.

[35] D. C. Pham, *Int. J. Solids Struct.* **2003**, *40*, 4911–4924.

[36] C. F. Cline, H. L. Dunegan, G. W. Henderson, *J. Appl. Phys.* **1967**, *38*, 1944–1948.

[37] H. S. Yoon, R. E. Newnham, *Acta Crystallogr. Sect. A* **1973**, *29*, 507–509.

[38] J. Singh, S. S. Sahoo, K. Venkatakrishnan, G. Vaitheeswaran, D. Errandonea, *J. Alloys Compd.* **2022**, *928*, 167178.

[39] M. Bouchenafa, A. Benmakhlouf, M. Sidoumou, A. Bouhemadou, S. Maabed, M. Halit, A. Bentabet, S. Bin-Omran, R. Khenata, Y. Al-Douri, *Mater. Sci. Semicond. Process.* **2020**, *114*, 105085.

[40] J. J. Lewandowski, W. H. Wang, A. L. Greer, *Philos. Mag. Lett.* **2005**, *85*, 77–87.

[41] S. F. Pugh, *The London, Edinburgh, and Dublin Philosophical Magazine and Journal of Science* **1954**, *45*, 823–843.

[42] R. E. Cohen, *Geophys. Res. Lett.* **1987**, *14*, 1053–1056.

[43] D. G. Pettifor, *Mater. Sci. Technol.* **1992**, *8*, 345–349.

[44] P. Ravindran, L. Fast, P. A. Korzhavyi, B. Johansson, J. Wills, O. Eriksson, *J. Appl. Phys.* **1998**, *84*, 4891–4904.

[45] D. H. Chung, W. R. Buessem, *J. Appl. Phys.* **1967**, *38*, 2010–2012.

[46] S. I. Ranganathan, M. Ostoja-Starzewski, *Phys. Rev. Lett.* **2008**, *101*, 55504.

[47] F. Gervais, B. Piriou, F. Cabannes, *Phys. Status Solidi B* **1973**, *55*, 143–154.

[48] V. Kovalev, V. Thomas, T. Setkova, N. Zubkova, A. Spivak, D. Fursenko, V. Yapaskurt, A. Antipin, E. Borovikova, *Phys. Chem. Miner.* **2023**, *50*, 20.

[49] T. Pilati, C. M. Gramaccioli, F. Pezzotta, P. Fermo, S. Bruni, *J. Phys. Chem. A* **1998**, *102*, 4990–4996.
[50] J. Jehlička, P. Vandenabeele, H. G. M. Edwards, *Spectrochim Acta A Mol Biomol Spectrosc* **2012**, *86*, 341–346.
[51] R. A. Morgan, F. A. Hummel, *J. Am. Ceram. Soc.* **1949**, *32*, 250–255.
[52] B. S. Hemingway, M. D. Barton, R. A. Robie, H. T. Haselton, *Am. Mineral.* **1986**, *71*, 557–568.
[53] I. R. Shein, R. Wilks, A. Moewes, E. Z. Kurmaev, D. A. Zatsepin, A. I. Kukharenko, S. O. Cholakh, *Phys. Solid State* **2008**, *50*, 615–620.
[54] G. E. Harlow, T. J. Shankland, *Geochim. Cosmochim. Acta* **1974**, *38*, 589–599.
[55] H. Hiramatsu, H. Yusa, R. Igarashi, Y. Ohishi, T. Kamiya, H. Hosono, *Inorg. Chem.* **2017**, *56*, 10535–10542.
[56] S. López-Moreno, J. Sánchez-Martín, E. Bandiello, M. Bettinelli, C. L. Bull, C. J. Ridley, D. Errandonea, *J. Phys. Chem. Solids* **2023**, *183*, 111604.

Manuscript received: November 27, 2023
Revised manuscript received: January 28, 2024
Accepted manuscript online: February 12, 2024
Version of record online: March 6, 2024